

One-dimensional moiré charge density wave in the hidden order state of URu_2Si_2 induced by fracture

Edwin Herrera,^{1,2,3} Víctor Barrena,¹ Isabel Guillamón,¹ José Augusto Galvis,³ William J. Herrera,² José Castilla,¹ Dai Aoki,⁴ Jacques Flouquet,⁴ and Hermann Suderow¹

¹*Laboratorio de Bajas Temperaturas y Altos Campos Magnéticos,*

Departamento de Física de la Materia Condensada,

Instituto Nicolás Cabrera and Condensed Matter Physics Center (IFIMAC),

Unidad Asociada UAM-CSIC, Universidad Autónoma de Madrid, E-28049 Madrid, Spain

²*Departamento de Física, Universidad Nacional de Colombia, Bogotá 111321, Colombia*

³*Facultad de Ingeniería y Ciencias Básicas,*

Universidad Central, Bogotá 110311, Colombia

⁴*Université Grenoble Alpes, CEA, INAC-PHELIQS, 38000 Grenoble, France*

(Dated: September 3, 2022)

Abstract

Moiré patterns can lead to fundamentally new electronic behavior when formed between two atomic lattices slightly shifted with respect to each other. A solid is however not just characterized by the atomic lattice, but also by charge or magnetic excitations that do not need to be commensurate to the lattice. This raises the question if one can obtain a moiré by combining periodic electronic modulations and the atomic lattice. Here we report on the discovery of a one-dimensional charge density wave (1D-CDW) whose wavevector is a moiré pattern between the atomic lattice and a hot spot for electronic scattering in the bandstructure of the hidden order (HO) state of URu_2Si_2 . The moiré is produced by fracturing the crystal at low temperatures. Our results suggest that charge interactions are among the most relevant features competing with HO in URu_2Si_2 .

The HO state of URu₂Si₂ puzzles experimentalists and theoreticians alike since its discovery more than three decades ago [8–10]. It consists of a phase transition below $T_{HO} = 17.5$ K in which there is a large entropy change[11]. In spite of intensive research and having scanned through nearly all available techniques, the actual order parameter associated to the entropy loss in the HO state, its symmetry and microscopic origin, remain in the dark[8–10]. Neutron scattering experiments do not show any sign of static magnetic nor structural order[12]. But there are two dynamical modes of Ising-like magnetic excitations with a strong associated magnetic moment, $\mu \approx 1 - 2\mu_B$, located at $q_0 = (0, 0, 1)$ and $q_1 = (0.6, 0, 0)$ [12–14]. Antiferromagnetism appears above 5 kbar with the q_0 wavevector[10, 12, 15]. The mode at q_1 [15, 16] leads at high magnetic fields to antiferromagnetic order with q_1 [17], after a set of modifications of the Fermi surface induced by the magnetic field which produce nesting in the Fermi surface at q_1 , when HO disappears[18]. Several measurements indicate that at zero field the bandstructure has a hot spot for scattering at q_1 [16, 18–20]. Here we use Scanning Tunneling Microscopy (STM) to study high quality single crystals of URu₂Si₂. Contrasting previous STM work[21, 22], we unambiguously identify a 1D-CDW with a very long wavevector that is a moiré combination of the atomic lattice and q_1 . We make detailed analysis of the sample surface after the experiment and find that the surface has linear features created during cleaving, which determines the reduced dimensionality of the CDW.

Figure 1(a) shows the crystal structure of URu₂Si₂ and in Fig. 1(b) we show atomically resolved images of the square atomic lattice. The spectroscopy will be discussed elsewhere and coincides with the expectations for a U surface, taking the results of [21–23]. The in-plane lattice parameter is of $a = 420 \pm 10$ pm.

We identify subtle nearly periodic changes of the height as a function of the position which lead to stripes in the STM images (Fig.2). In fields of view that are sufficiently large and free of defects, there is a certain pattern which repeats on the image and is one-dimensional. The pattern corresponds to height changes which vary from place to place and are very small, of at most 2 pm, i.e. about 1% of a typical atomic size or a fraction of the usual atomic corrugation (inset of Fig. 1b). The period and the direction of the one-dimensional modulation can be determined from the Fourier transforms of the topographic images. The Bragg peaks associated to the one-dimensional modulation repeat at integer multiples of q_M . We determine q_M from the reciprocal space distance between consecutive peaks and obtain that $q_M = 0.171/\text{nm}$ (Fig.2b). This corresponds to an electronic modulation of period

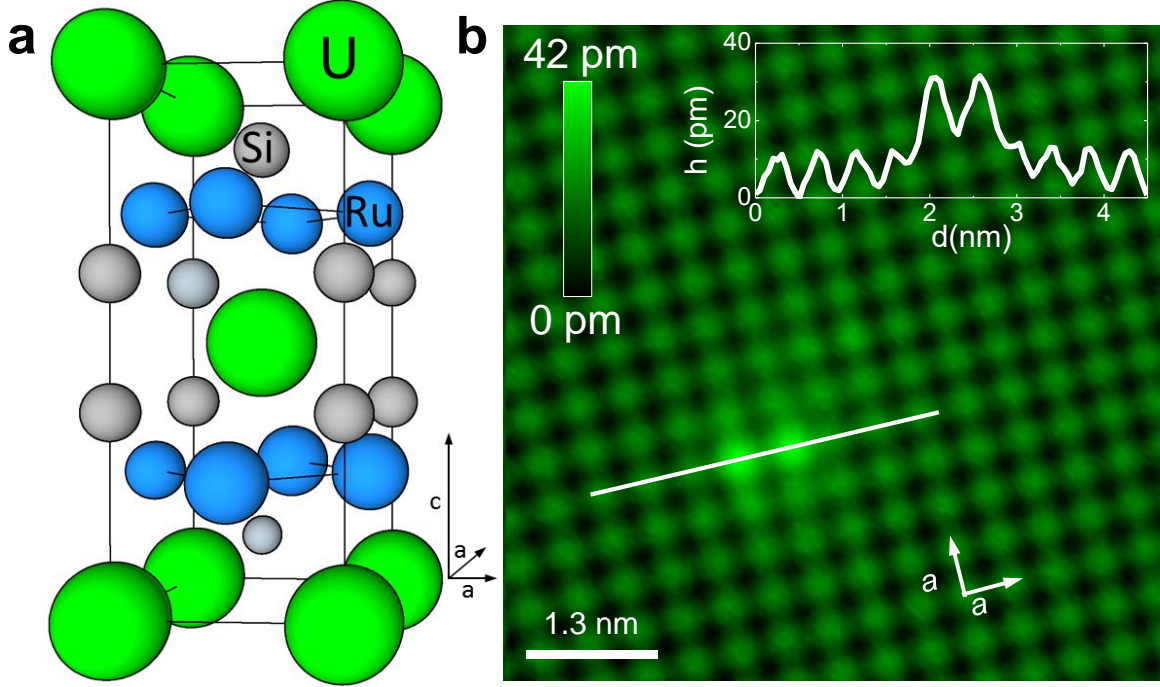


FIG. 1. **Atomic size STM images of the square in-plane lattice in URu_2Si_2 .** **a** URu_2Si_2 tetragonal crystalline structure ($a = 420$ pm and $c = 960$ pm), with U atoms in green, Ru atoms in blue and Si atoms in grey. **b** Atomic resolution STM image showing the square U surface. A defect consisting of a couple of atomic size features is seen in the image. The white line provides the direction of the scan shown in the inset (upper right). Arrows show the crystalline directions and the color scale the height difference, following the color bar on the upper left.

$d_M = 1/q_M = 6$ nm ($d_M = 14a$). The determination of d_M is limited by the width of the peak in Fourier space, which corresponds about ± 1 nm in real space. The one-dimensional modulation is nearly parallel to an in-plane crystalline direction, at an angle δ of a few degrees. A histogram with observed d_M and δ is shown in Fig. 2c. The modulation consists of fringes with periodicity d_M in real space and at q_M in the Fourier transform. The peaks q_M are mostly located around the center, but sometimes repeat at the atomic lattice Bragg peaks. We did not find significant changes below about 10 mV. We observed the modulation up to magnetic fields of 4 T and temperatures several K above liquid helium. At higher temperatures and above T_{HO} we were unable to detect it because of temperature induced drift in the STM.

A modulation observed in STM superimposed to the atomic lattice is caused by charge

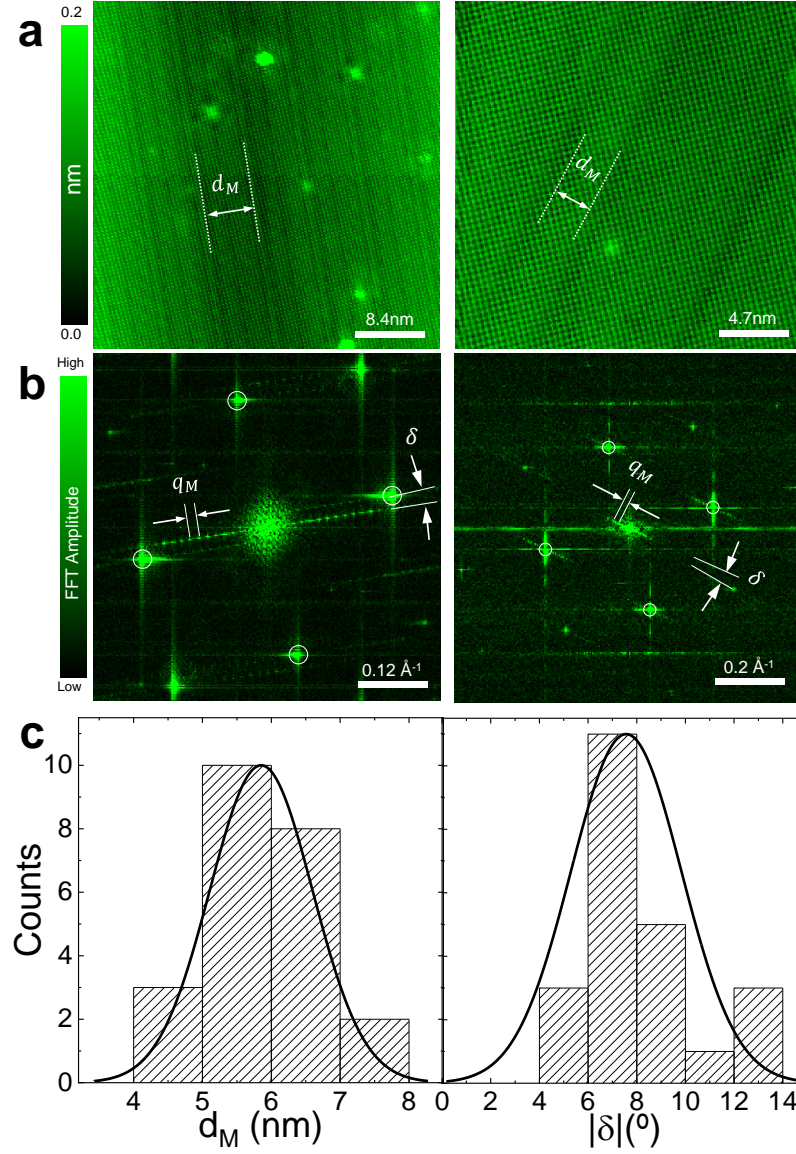


FIG. 2. **Moiré 1D-CDW in URu_2Si_2 .** **a** Atomic resolution STM images in two different fields of view. Notice that these are considerably larger than those in Fig. 1. We mark the one-dimensional modulation of size d_M by dashed lines and the arrow. **b** Fourier transform of the same images. We observe the usual atomic Bragg peaks due to the square surface atomic lattice and also multiple peaks at reciprocal space distances q_M . We mark in white the angle δ between the modulation and the Bragg peaks of the atomic lattice. In **c** we show a histogram over d_M and angles δ obtained in 24 different fields of view acquired in 5 different samples. We collect the position in Fourier space of the maximum of the peak, giving q_M . The peak has however a certain width, which corresponds to a distance of about 1 nm in real space.

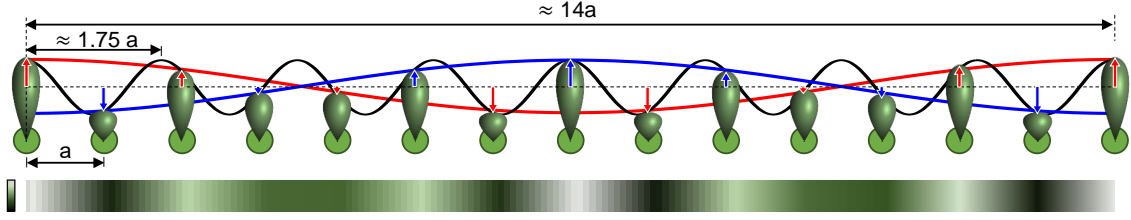


FIG. 3. **Schematic of the moiré 1D-CDW.** We represent the atoms in green in form of a single orbital, whose elongation in z is coupled to a modulation located at the reciprocal lattice vector $q_1 = 0.57 \approx 0.6$ (black line, $\lambda_1 \approx 1.75a$ in real space, with $a = 420$ pm). The elongation is highlighted by a colored arrow at each atomic position. We represent the resulting charge modulation using a color scale by the bar at the bottom. The wavevector of the modulation is q_M ($\lambda_M \approx 14a$ in real space). Because $\lambda_1/2 \approx a$, the relation between λ_1 and a is through a "fractional" moiré $\lambda_M = \frac{\lambda_1 \cdot a}{|\lambda_1/n - a|}$ with $n = 2$ and the pattern is formed by two cosine waves with the same wavelength, but shifted by π from each other (red and blue).

order in form of a CDW. The Fermi surface has mainly a four-fold symmetry and there are no features in the Fermi surface which could lead to any 1D-CDW[19, 24]. Features of the Fermi surface are instead fourfold, showing nesting at q_0 . Nesting occurs at q_1 too at sufficiently high magnetic fields[18]. At the level of the local atomic size density of states measured by STM, one could eventually expect some sort of modulations appearing at these wavevectors. In any case, we would not be sensitive to q_0 , which is out-of-plane, because we observe the in-plane square atomic lattice. But we should be sensitive to an excitation at q_1 , such as a hot spot in the Fermi surface or a van-Hove anomaly. As we show in the following, q_M is related to q_1 through a moiré pattern and the direction of q_M is determined by the direction of the propagation of the crack front during fracture.

First, let us establish the relation between q_1 and q_M , knowing that $q_1 \gg q_M$. The superposition of 1D modulations with similar periodicities λ_1 and λ_2 ($\lambda_1 \approx \lambda_2$) leads to an additional modulation, the moiré pattern, at a scale which is far above λ_1 and λ_2 and is given by $\lambda_M = \frac{\lambda_1 \cdot \lambda_2}{|\lambda_1 - \lambda_2|}$ [25, 26]. If $\lambda_2 = a$ and $\lambda_1 \approx na$ with n an integer (and of course $\lambda_1 \neq na$), the moiré adopts a "fractional" form and $\lambda_M = \frac{\lambda_1 \cdot a}{|\lambda_1/n - a|}$. The moiré is then composed of

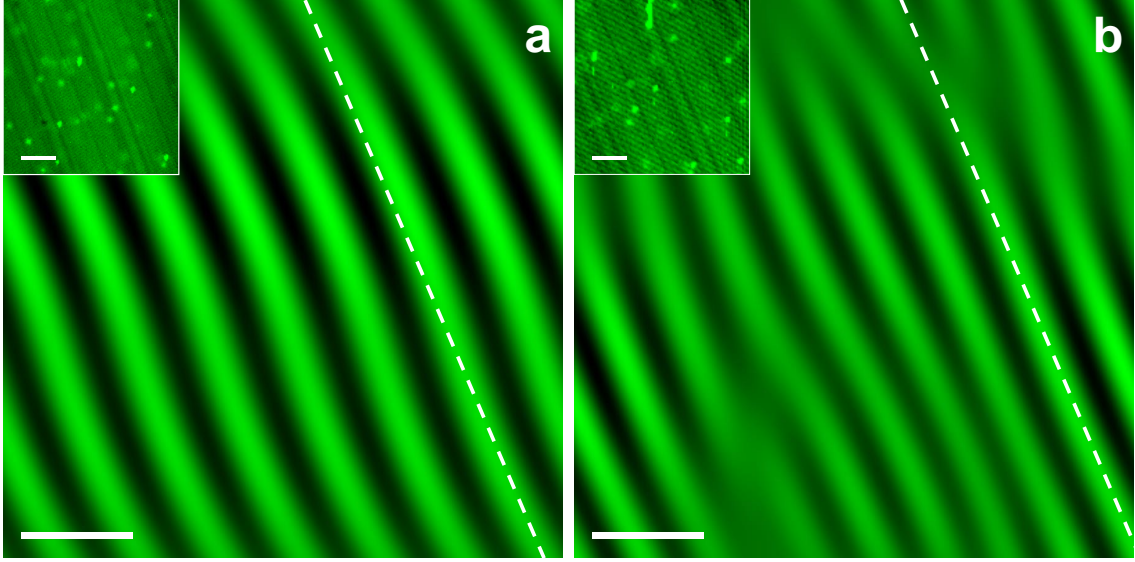


FIG. 4. **Defects in the moiré 1D-CDW.** In **a** and **b** we show two fields of view where we have Fourier filtered the first Bragg peaks of the modulation. The corresponding images are shown in the insets. White dashed lines are guides to the eye following linear features. We see that in **a** there is a shift, due to a defect in the modulation and in **b** there are dislocations. White scale bars are 10 nm long.

n cosine functions of wavelength λ_M phase-shifted to each other by $2\pi/n$. In STM images made at constant tunneling current, we measure the variations in the local density of states integrated between the Fermi level and the bias voltage as a function of the position. The local density of states can be understood as a combination of localized orbitals and itinerant electrons[27, 28]. Let us take for simplicity the case of a 1D row of atoms, separated by a given lattice constant. If there is a very weak modulation at a wavevector close to an integer times the lattice constant superposed to the 1D atomic lattice, the visible signature of this modulation on the local density of states is formed by the moiré pattern resulting from the value of the modulation at the atomic lattice positions. Let us consider schematically a set of elongated atomic orbitals located at a and assume that the size of the lobes is given by a modulation close to q_1 (at $\approx (0.57 \ 0 \ 0)$, which gives $\lambda_1 \approx 2\lambda_2$, with λ_1 the modulation at q_1 , $\lambda_1 = 1/q_1$, and $\lambda_2 = a$). The result is schematically shown in Fig. 3. The size of the lobes leads to a pattern which consists of two inverted cosines, each one with a periodicity

$\lambda_M = \frac{\lambda_1 \cdot a}{|\lambda_1/2 - a|}$ and shifted by π . Thus, our images show CDW at λ_M as a consequence of a moiré combination between q_1 and the atomic lattice.

Second, to understand the symmetry breaking, let us discuss the origin of the modulation. The modulation is not present in any of the STM images shown in Ref.[21, 22], although their resolution was of the same order as ours. In those experiments, cleavage was made at relatively high temperatures (of the order of liquid nitrogen), whereas we cleave our sample at very low temperatures (below liquid helium). Cleavage of a hard single crystal is equivalent to brittle fracture. It is a violent procedure by which the bonds are broken first on one side of the sample and then a crack front travels through the sample. The propagation of the crack front during cleavage leaves permanent modifications of the surface[29]. These modifications can be due to acoustic waves that are emitted when a crack front crosses defects during the cleaving process or due to other forms of local interaction of the crack front and the crystalline lattice and have been extensively studied in materials such as Si, sapphire or tungsten[29–32]. A careful optical and electron microscopy analysis of surfaces of URu₂Si₂ broken at room temperatures and at low temperatures is provided in the Supplementary Information. We show how the surface of samples cleaved at low temperatures has characteristic one-dimensional stripes. These stripes define a fixed direction which is close to one of the main in-plane crystalline axis and produce the one-dimensional symmetry breaking field.

Before further analyzing the modulation, let us note that the broken surface could in principle also lead to a CDW at q_1 directly, and not in form of a moiré pattern resulting from the interaction of charge order and the atomic lattice. It seems however very unlikely that five samples cut differently, each one with slightly different shapes, different crack initiation points, and different internal structure of defects all lead to the same q_M .

A charge modulation also implies defects in the modulation[33]. Such a situation occurs in Fig. 4, where we filter the peaks corresponding to the modulation at q_M to obtain Fig. 4**a,b**. We observe that, in these fields of view, the stripes are structured. In Fig. 4**a** there is a shear shift of the charge modulation. In Fig. 4**b** there is a pair of dislocations in the charge modulation in the top of the image and another dislocation in the bottom of the image.

Most of our scans show the 1D-CDW Bragg peaks just at the center of the Fourier transform. To understand this observation, let us describe a CDW through a vector $\mathbf{D}(\mathbf{r}) = \mathbf{A} \cos(\mathbf{q}\mathbf{r} + \phi)$, with \mathbf{A} the vector of the absolute value of the modulation, \mathbf{q} the wavevector of the modulation and ϕ a phase shift. As we show in the Supplementary Information, the

corresponding Fourier transform shows satellite peaks around lattice Bragg peaks when the displacement vector is in-plane along $\mathbf{A} = (A_0, 0, 0)$ or $\mathbf{A} = (0, A_0, 0)$. If the displacement is out-of-plane, $\mathbf{A} = (0, 0, A_0)$, the image shows satellite peaks around the center of the Fourier transform. Thus, we are mostly observing an amplitude modulation of the charge (out-of-plane), without in-plane atomic displacements.

Notice however that sometimes we do observe the 1D-CDW in the Fourier transform around atomic Bragg peaks too. Then, the modulation locks to crystalline defects which lead to a twist (Fig. 4). The defects in the modulation are phase slips in the charge density vector $\mathbf{D}(\mathbf{r})$ by $\phi = 2\pi$ around a pair of dislocations and lead to small atomic lateral displacements.

Thus, the 1D-CDW at q_M is the result of a strong interaction between an external action (crack front), atomic displacements (phonons) and the electronic susceptibility of URu_2Si_2 (fluctuations at q_1). The phonon dispersion in URu_2Si_2 shows no strong features connected to the HO transition[34]. However, there is an anomalous phonon mode broadening which suggests strong anharmonicity and coupling to magnetic excitations[34–36]. The dispersion relation of the q_1 modes provides a velocity $v = \frac{dc}{dk} \approx 10^4 \frac{m}{s}$ [34]. Most remarkably, crack front velocity, sound velocity and the velocity of the magnetic q_1 modes are all of the order of tens of km/s.

Interestingly, the time required for each of these three modes to cross a single unit cell is in the femtosecond regime. Thus, ultrafast radiation experiments on surfaces of URu_2Si_2 might lead to similar effects as a travelling crack front and potentially to the nucleation of a similar CDW.

Notice that moiré patterns arise on surfaces or few layer systems because of displacements or rotations of atomic lattices[1–7]. Rotations among atomic layers provide a control parameter, the relative angle between layers, to modify the moiré[2]. In our case, moiré modulations can arise with any characteristic vector from the electronic bandstructure. That is, with wavevectors located inside the Brillouin zone and lying close to an integer fraction of the unit cell lattice. To modify the moiré, we need to modify the bandstructure, with the usual control parameters as doping, stress or magnetic field.

For very large values of n in $\lambda_M = \frac{\lambda_1 \cdot a}{|\lambda_1/n - a|}$, the moiré pattern might rapidly acquire a very long wavelength, which should make it quite difficult to distinguish from a large defect or distortion. However, for small n (and with a sufficient difference between λ_1 and na), the

moiré combinations proposed here could lead to a variety of new ground states.

In summary, we observe that the high susceptibility of URu_2Si_2 at q_1 results in quenched 1D-CDW when there is a sufficiently strong interaction with a cracking process. But we are not just condensing a CDW related to q_1 through fracture. The moiré between the atomic lattice and the q_1 modulation leads to a real, physical, 1D-CDW which breaks the in-plane square C_4 symmetry. Of course such a CDW is not a property of the HO. But it emerges from HO, and it emphasizes the proximity to competing ground states. Our observation supports the claim that in the HO phase electric interactions might play a key role, as proposed by nuclear magnetic resonance experiments[37].

ACKNOWLEDGMENTS

We acknowledge discussions with F. Guinea, A. Levy Yeyati and with S. Vieira. This work was supported by the Spanish MINECO (FIS2014-54498-R, MDM-2014-0377), by the Comunidad de Madrid through program NANOFRONTMAG-CM (S2013/MIT-2850) and by Cost Action CA16218 (NanocoHybri). I.G. acknowledges support by the European Research Council PNICTEYES grant agreement 679080. We also acknowledge the support of Departamento Administrativo de Ciencia, Tecnología e Innovación, COLCIENCIAS (Colombia) Convocatoria 784 - 2017 and the Cluster de investigación en ciencias y tecnologías convergentes de la Universidad Central (Colombia). We also acknowledge SEGAINVEX at UAM.

METHODS

We use a STM set-up described in Refs.[38, 39] that features a movable sample holder which we use to cleave in-situ the sample. The single crystals of URu_2Si_2 have been grown by Czochralski method and have a residual resistance ratio of about 120 [40]. We first screened crystals for high quality, from different growths and then cut crystals into needles of about $0.5 \text{ mm} \times 0.5 \text{ mm} \times 2 \text{ mm}$. We inserted each needle into a hole made on a gold substrate and glued them with silver epoxy. The needles were positioned into the sample holder in such a way that they hit a sharp ceramic blade when pulling on the sample holder. Slightly below 4.2 K we pulled on the holder through a manual mechanism located at room temperature and connected to the holder with a piano cord. We felt resistance when the

sample touched the blade. We continued pulling until we heard a characteristic "crack". At this point, the sample was broken. The noise created during crack, which we heard outside the dilution refrigerator, evidences generation of sound waves during fracture. This was made with the tip far from the sample. We then approached the tip to the sample, scanned and obtained the results discussed here. We provide results obtained in five succesful cleaves, obtaining each time atomically flat surfaces in cryogenic vacuum. In each crystal, we were able to study several tens of scanning windows, each limited by the scanning range of our piezotube ($2\mu\text{m} \times 2\mu\text{m}$)[38]. We present images made at 150 mK and with the STM on constant current mode held by a feedback loop, with a setpoint of a fraction of nA and at a bias voltage of order of 10 mV.

SUPPLEMENTARY INFORMATION

A. Further details of the experimental set-up

The STM set-up has been described in detail elsewhere[38]. However, it is useful to provide details about the additions that we have made to be able to cleave at low temperatures hard samples as URu_2Si_2 . In Fig. 5a we show a picture of URu_2Si_2 from the side and from the top. The sample has been specifically shaped using a wire saw into a rectangle elongated perpendicular to the cleaving plane (the (a,a) axis). In Fig. 5b we show a picture of the sample mounted on the STM. The picture is taken from one side. The piezotube is located on the top of the picture. We can see the tip of Au on the top of the image and the part of the URu_2Si_2 that holds out from the sample holder. A cleaved surface is shown in Fig. 5c from the top. In Fig. 5d we schematically show the process of cleaving. We move laterally the sample holder and a ceramic blade pushes laterally the rectangular sample until it breaks. The efforts during the crack are tear, compressive and shear efforts, as schematically represented in Fig. 5e.

The tip of Au is prepared and shaped as shown in Refs. [38, 41]. To this end, we glue a pad of Au on the sample holder in such a way that we can move the tip between sample and pad of gold, once the sample has been cleaved. To analyze the images we use WSxM [42] and further software available at [43].

B. Analysis of fractured surfaces

After the experiment, we verified that the only source for the cracking noise was the sample (no components of the dilution refrigerator or the STM were damaged). The remaining part of the sample generally flew away to the bottom of the vacuum chamber. We collected both parts of the sample and made a detailed analysis of their surface using Scanning Electron Microscopy (SEM) and optical microscopy at room temperature.

In single crystals, fractures are the result of the external applied stress, the elastic properties of the crystal and the relative orientation between the crack propagation and the crystalline lattice directions. As a result, characteristic surface marks can be identified to reconstruct the fracture process. We have made a microscopy study of surfaces on URu_2Si_2 obtained after cleaving at room temperature and at low temperatures (Fig. 6). We iden-

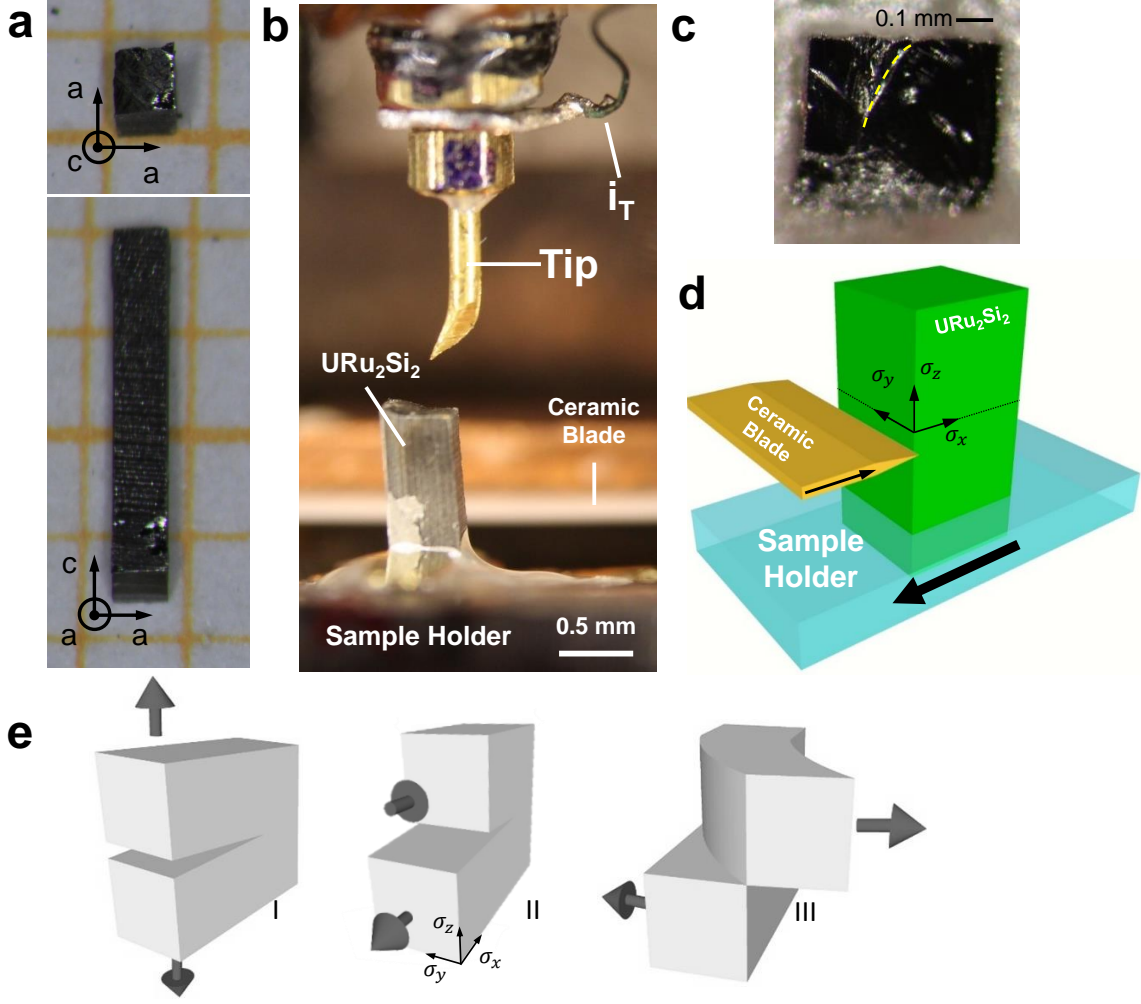


FIG. 5. **Method used to cleave the URu_2Si_2 single crystals.** In **a** we show a sample of URu_2Si_2 from the side (bottom) and from the top (top). We mark the crystalline axes with arrows. The sample has been cut using a wire saw. In **b** we show the sample mounted on the STM at room temperature. The sample is glued using silver epoxy on the sample holder. The tip of Au is positioned on the top of the sample. After cleaving at liquid helium temperatures, the tip moves using a piezoelectric motor down to tunnel into the broken sample (not shown). We also mark the wire for the tunneling current. The contact to the sample is made through the sample holder. The ceramic blade is also seen. It is located (out of focus in the picture) behind the sample. In **c** we show a photography of a sample broken at low temperatures, surrounded by the silver epoxy. The yellow dashed line is a large defect inside the crystal. At low temperatures, the sample holder is moved towards the blade, as shown in **d**. The efforts made on the sample are shown in **e** and consist of tear (mode I), compression (mode II) and shear (mode III). In **d,e** we mark the corresponding stress $\sigma_{x,y,z}$ as black arrows.

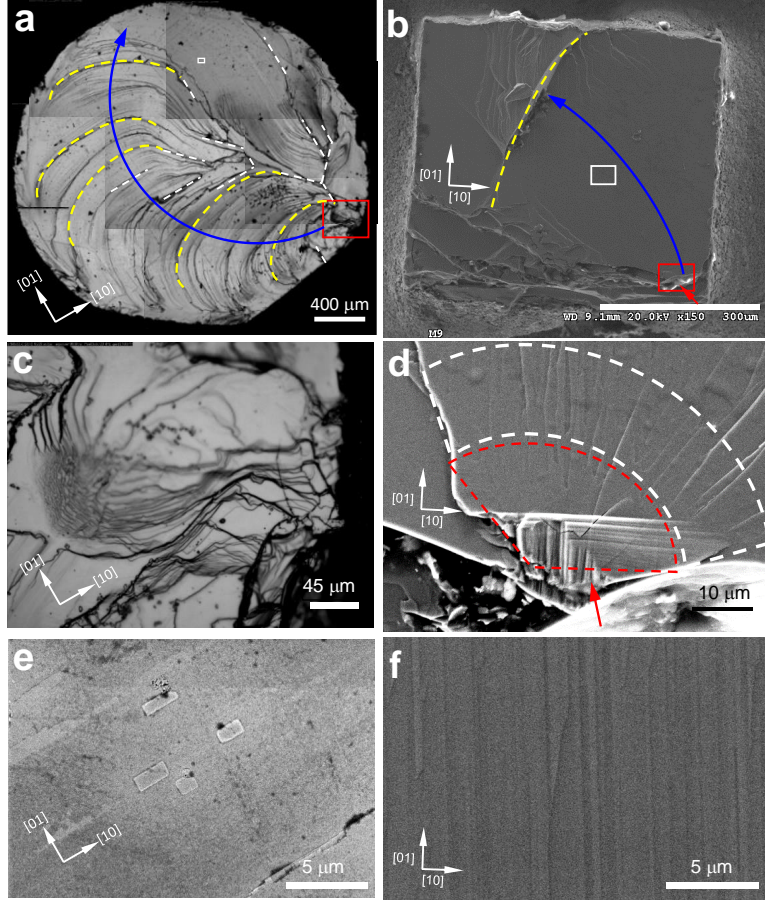


FIG. 6. **Analysis of surface marks after cleaving.** In **a,c,e** we show pictures of a sample cleaved at room temperature and in **b,d,f** of a sample cleaved at liquid helium. In **a** we show a large scale optical image of the sample. We mark by a blue arrow the path of the crack front. Yellow lines mark remarkable features formed during crack. With a red rectangle we mark the place where the crack started. An optical image of the red rectangle of the room temperature cleaved sample is shown in **c**. A zoom of the region marked by a small white rectangle in **a** is shown in **e**. Notice the presence of defects, but of no well-defined pattern. In **b** we show a SEM image of the sample cleaved at liquid helium temperatures. We mark the region where the crack started by a red rectangle. A zoom of this area is shown in the SEM image **d**. A red arrow identifies the point where the crack started. The dashed red region is the so-called mirror zone, which appears prior to the zone where the crack produces twist hackles distributed radially (white dashed lines). These then proliferate through the sample and tend to align to the crystalline axis. In **f** we show the region on a white rectangle of **b**. We can identify a strongly one-dimensional pattern, which is absent in the other sample (**e**). Arrows in each image provide the crystalline directions. Scale bars are shown in white.

tify with yellow dashed lines step hackles. In both cases, hackles follow an elliptical shape. The crack front travels along a direction perpendicular to the hackle lines[31, 32, 44]. The curved crack direction results due to the deflection of the crack between planes because of the anisotropic velocity dependence of lattice vibrations[30]. In our case, the crack front in the sample cleaved at room temperature can be approximated by an ellipse of semi-axes of $a \approx 2.06\text{mm}$ and $b \approx 2.73\text{mm}$. From such a simple shape we can estimate the propagation velocity of the crack front to be of order of 10^3 m/s [31, 32, 44]. The sample cleaved at low temperatures is too small to make an estimation, but we can expect similar crack front velocities.

In the sample cleaved at room temperature we found that it was not easy to identify the starting crack point. Instead we observe a starting crack zone of approximately a few μm^2 (red rectangle in Fig.6a and Fig.6c). By contrast, on the sample cleaved at low temperature, we identify the starting crack point as the red arrow in Fig.6d. In every crack, we can identify the primary surface marks, called mirror and mist zones. These are regions where a crack radiates outwards from the starting point of fracture. These zones are the transition regions between the starting crack point and the hackle lines. We define the mirror zone by the region enclosed by the red dashed line (Fig.6d). Inside the mirror zone we identify radially outgoing lines. Outside, in the mist zone, lines start to become straight and oriented with the crystalline axis, ending up in hackle lines. Hackle lines run in the local direction of cracking and separate parallel but non coplanar sections of the fractured surface. Twist hackles are formed when the crack runs parallel to a preferential cleaving plane and the direction of the normal stress to this plane changes. Then, the crack cannot tilt in response to the new direction of stress direction and thus it splits into small, separated segments[45]. These lines form at exactly 90° to each other and are often close to being parallel to a crystalline axis. The lines evidence the large accumulation of strain before the crack (see also Fig.7).

In order to address with more accuracy the crack features on the cleavage surfaces on both samples, we focus our attention in areas less than $25 \times 25 \mu\text{m}^2$ (Fig.6e,f). There we can observe important differences. In the sample cleaved at room temperature we identify flat surfaces of tens of microns with rectangular defects within areas of sizes $1\text{-}2 \mu\text{m}^2$ that are parallel to the [10] and [01] directions (Fig.6e). In the sample cleaved at 4.2K, by contrast, we observe stripes nearly parallel to the [01] atomic direction (Fig.6f). This suggests that there

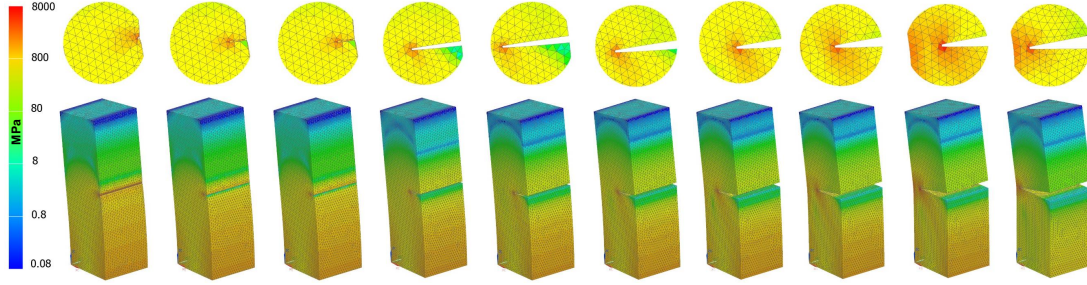


FIG. 7. **Simulations of the distribution of pressure in the sample during fracture.** We show a beam with a similar geometry as the original URu_2Si_2 sample. The color scale in all samples represents the pressure distribution in MPa. The black lines are the mesh used in finite element calculations of the local pressure. The pressure is given by the color scale on the left. Force is applied on the top part of the sample. The wedge opens from left to right, the latter image being just prior to fracture. On the top we see a view of the fracture position for each image of the sequence. Notice that pressure is strongly built up on the wedge, which travels as a crack front through the surface.

is a hierarchy of structures appearing at low temperatures caused by the crack process. Stripes that define a direction and the interaction of the crack front with the modes of URu_2Si_2 that defines a charge modulation condensed during the crack process.

The establishment of any permanent modification of the crystal structure requires energy. The only available source is the strain energy dissipating during cleavage, which is used to create the new surfaces obtained after cleaving. It is useful to discuss the strain we accumulate before breaking the sample. To see this, we can consider that, when we use samples of 1 mm square section (instead of 0.5 mm), we break a tin solder joint of the pulling mechanism instead of the sample. By decreasing sample thickness to 0.5 mm we break instead the sample. Thus, we can estimate that the uniaxial force on the sample is of order of the shear force of a tin solder joint. A good estimate is probably between 1 and 10 kg, say 5 kg or 50 N. This is applied as a shear to the sample using a wedge. The uniaxial pressure is as high as 200 kg/mm^2 , if we estimate that contact between the wedge and the sample is along an area of $0.1 \times 0.5 \text{ mm}^2$. This produces as much as 20 kbar uniaxial pressure, enough to locally drive the system into an ordered phase close to the wedge[9, 10]. A more detailed calculation is provided in Fig. 7. We use a finite element calculation with the

software NX Nastran. We use isoparametric tetrahedron elements with four vortex nodes and size additional midside nodes. The sample size is $1\text{ mm} \times 1\text{ mm} \times 3\text{ mm}$ and the mesh size is $50\mu\text{m}$. We apply a lateral force of 50 N and a vertical tear force of 100 N, to be able to consider a sample separated in two parts in the model. We take a Young modulus of 192.85 GPa[11]. We see that we can easily obtain locally pressures up to 80 kbar (8 GPa) at the wedge (Fig. 7).

When the sample cleaves, the pressure is of course released, so that the sample should turn back to the HO state. However, there is a large amount of available energy from the accumulated strain. We can estimate the released energy and compare it to the bonding energy and find very large values, of order of the mJ. On the other hand, usually the tensile strength upon shear of the material is exactly the bond-breaking strength, plus the energy required to produce surface modifications. To have such a surplus of mechanical energy that does not go into bond-breaking and creates permanent features on the surface, we need that the lateral edge of the sample has a higher tensile strength than the bulk. This should indeed be the case, taking into account that the sample has been cut and has certainly many more defects close to the edge. As we see in Fig. 6, the surfaces obtained from cleaving an as-grown sample at room temperature are very different than those obtained cleaving a sample shaped using a wire saw at low temperature. The latter shows many more small scale modifications of the surface. Thus, the crack process has enough energy to produce permanent modifications of the surface. Furthermore, the local accumulated pressure drives the sample out of the HO state for the duration of the propagation of the crack front through the sample.

C. Displacement vector and bias voltage dependence

As we show in Fig. 8, the Fourier patterns of displacement vectors with different directions are different too. We take $\mathbf{D}(\mathbf{r}) = \mathbf{A}\cos(\mathbf{q}\mathbf{r} + \phi)$, as in the main text. In Fig. 8a we show a height modulation, equivalent to the charge modulation observed in the main text (with a period of λ_M , for simplicity, we take here a single cosine, instead of the two cosines leading to the moiré pattern discussed in the text). The corresponding pattern consists of stripes and in the Fourier transform Fig. 8g we observe peaks around the center. When there is an in-plane displacement (Fig. 8b), the peaks in Fourier space appear around the Bragg peaks

of the unmodulated atomic lattice, without peaks at the center of the Fourier transform. If we combine both modulations, by adding a z and an in-plane modulation in Fig. 8c, and add a tilt, we observe the patterns in Fig. 8i, with peaks around the center and the Bragg peaks of the unmodulated atomic lattice. Thus, as suggested in the text, the observation of peaks around the atomic size Bragg peaks shows that there are in-plane displacements, in addition to the charge order. This occurs preferentially at locations where the observed charge modulation shows defects, as discussed in the text.

In Fig. 9 we show the bias voltage dependence of the modulation discussed in the main text. We focus on the range between 10 mV and 2 mV. Real space images show the modulation and a few defects. The Fourier transform shows the four Bragg peaks of the atomic lattice and the peaks corresponding to the q_M modulation. In Fourier space we also observe a white circle, with structure inside, around the center. This is the consequence of quasiparticle interference scattering at the defects. Here we show topographic images, which are obtained at constant current. The current is given by $I(V) \propto \int_0^{eV_B} dE N(E - eV)$ where V_B is the bias voltage given in the images and $N(E)$ the density of states. Therefore, it provides an energy integrated account of the density of states between zero bias and the voltages mentioned at each image in Fig. 9. The quasiparticle interference does not provide qualitative information from the bandstructure. Rather, scattered features that are difficult to interpret. To this end, doping with Th, as made in Ref. [22] is very important. Other features of the spectroscopy will be discussed elsewhere, but essentially coincide with what was found in Refs. [21, 22]. We did not find clear features in the spectroscopy associated to the CDW at q_M found here. This might not be surprising. The fact that the observed corrugation is so small, considerably smaller than the signal from scattering (Fig. 9) suggests that the associated features in $N(E)$ are very small too. Furthermore, the local density of states has no region in energy where it is flat. It consists of a Fano anomaly, superposed to a gap opening and of two van Hove singularities located at a few mV [21, 22]. Any feature appearing in such a wavy background is very difficult to disentangle. However, the q_M modulation appears at a range of bias voltages of order of the tens of mV and below.

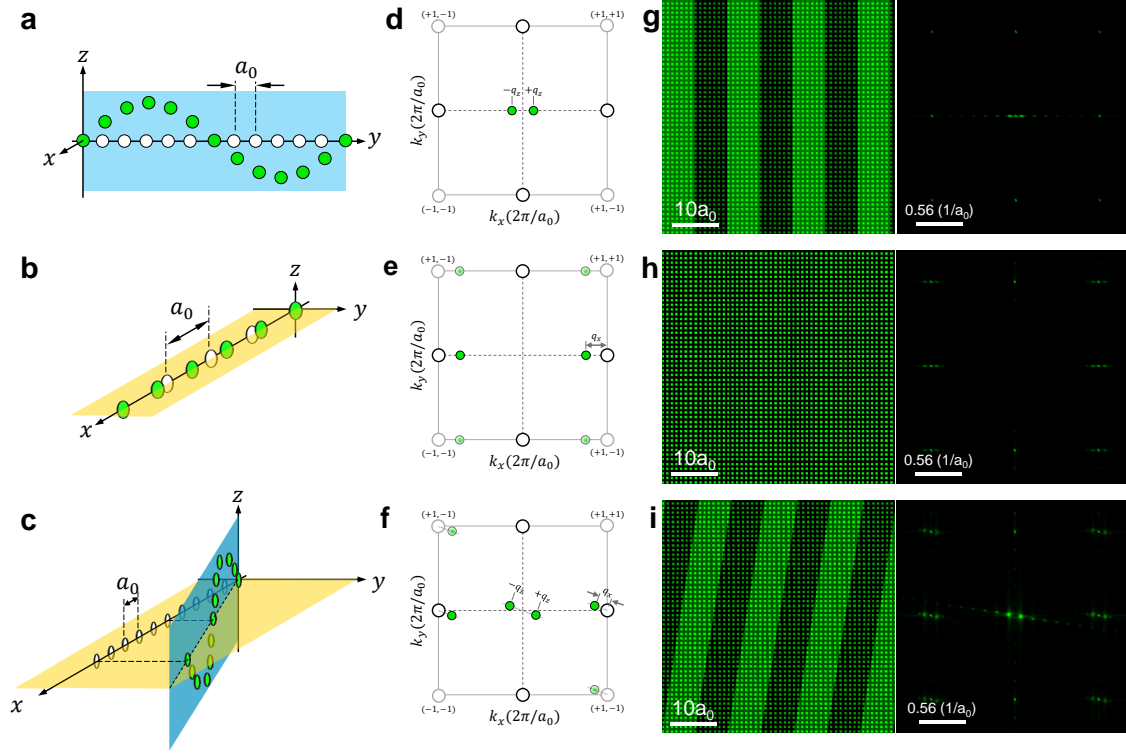


FIG. 8. **Displacement vector in real and reciprocal space.** Schematic representation of a real space modulation for atomic displacements in a square atomic lattice. White circles show atomic positions without perturbation and green circles with a sinusoidal perturbation. In **a** the perturbation is along the z -axis, out of plane. In **b** we show a longitudinal modulation along the x -axis. In **c** we show a modulation out of plane with a q vector slightly tilted in plane. The positions in reciprocal space of the Bragg peaks in the Fourier transforms are shown in **d,e,f**. White dots are the atomic Bragg peaks. Green dots show the positions of the perturbed situations. Notice that peaks appear at the center of the Fourier transform only when there is an out of plane modulation. A simulation using a 2D lattice is shown in real and reciprocal space in **g,h,i**.

-
- [1] R. Bistritzer and A. H. MacDonald, *Moiré bands in twisted double-layer graphene*, Proceedings of the National Academy of Sciences **108**, 12233 (2011), <https://www.pnas.org/content/108/30/12233.full.pdf>.
- [2] Y. Cao, V. Fatemi, A. Demir, S. Fang, S. L. Tomarken, J. Y. Luo, J. D. Sanchez-Yamagishi,

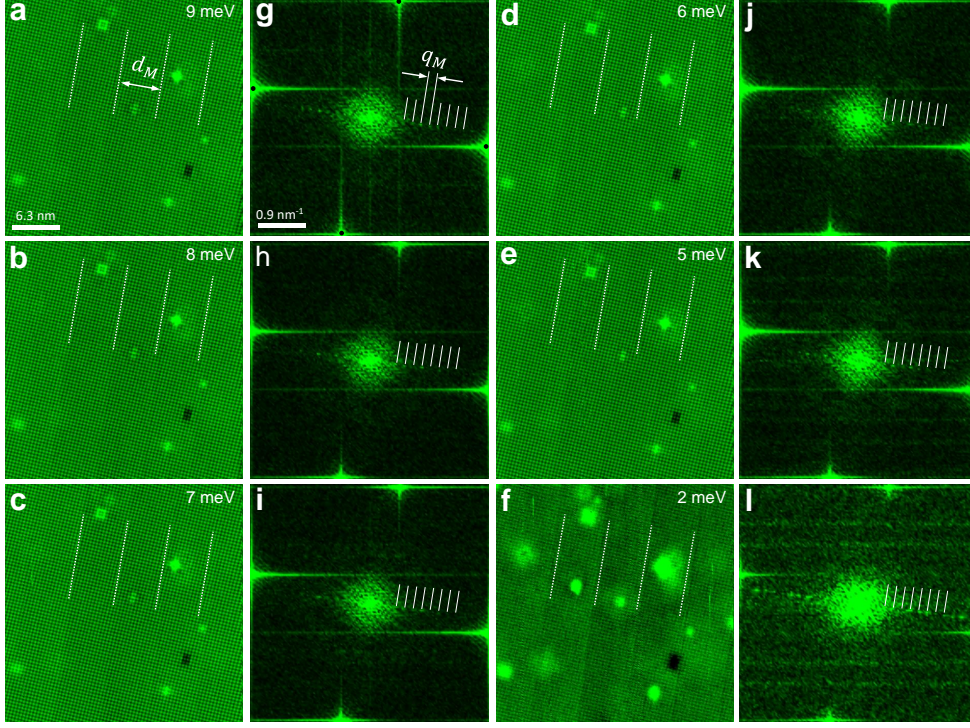


FIG. 9. **Bias voltage dependence of the 1D-CDW.** **a** shows atomically flat images made at the bias voltage marked on the top right part of the image. We mark the modulation at d_M by white dashed lines. Scale bar is on the bottom left. In **g** we show the corresponding Fourier transform, with the scale bar on the bottom left. We highlight the Bragg peaks of the crystal lattice by dark points and by white dashed lines the modulation wavevector q_M . This is repeated for different bias voltages in the other panels (**b,h** to **f,l**).

- K. Watanabe, T. Taniguchi, E. Kaxiras, R. C. Ashoori, and P. Jarillo-Herrero, *Correlated insulator behaviour at half-filling in magic-angle graphene superlattices*, Nature **556**, 80 (2018).
- [3] Y. Xie, B. Lian, B. Jäck, X. Liu, C.-L. Chiu, K. Watanabe, T. Taniguchi, B. A. Bernevig, and A. Yazdani, *Spectroscopic signatures of many-body correlations in magic-angle twisted bilayer graphene*, Nature **572**, 101 (2019).
- [4] Y. Choi, J. Kemmer, Y. Peng, A. Thomson, H. Arora, R. Polski, Y. Zhang, H. Ren, J. Alicea, G. Refael, F. von Oppen, K. Watanabe, T. Taniguchi, and S. Nadj-Perge, *Electronic correlations in twisted bilayer graphene near the magic angle*, Nature Physics **15**, 1174 (2019).
- [5] Y. Jiang, X. Lai, K. Watanabe, T. Taniguchi, K. Haule, J. Mao, and E. Y. Andrei, *Charge order and broken rotational symmetry in magic-angle twisted bilayer graphene*, Nature **573**,

91 (2019).

- [6] X. Lu, P. Stepanov, W. Yang, M. Xie, M. A. Aamir, I. Das, C. Urgell, K. Watanabe, T. Taniguchi, G. Zhang, A. Bachtold, A. H. MacDonald, and D. K. Efetov, *Superconductors, orbital magnets and correlated states in magic-angle bilayer graphene*, Nature **574**, 653 (2019).
- [7] L. Peng, J. Qiao, J.-J. Xian, Y. Pan, W. Ji, W. Zhang, and Y.-S. Fu, *Unusual electronic states and superconducting proximity effect of Bi films modulated by a NbSe₂ substrate*, ACS Nano **13**, 1885 (2019), <https://doi.org/10.1021/acsnano.8b08051>.
- [8] J. Flouquet, *On the heavy fermion road*, Progress in Low Temperature Physics **15**, 139 (2005).
- [9] J. A. Mydosh and P. M. Oppeneer, *Colloquium : Hidden order, superconductivity, and magnetism: The unsolved case of URu₂Si₂*, Rev. Mod. Phys. **83**, 1301 (2011).
- [10] J. A. Mydosh, P. M. Oppeneer, and P. S. Riseborough, *Hidden order and beyond: an experimental—theoretical overview of the multifaceted behavior of URu₂Si₂*, Journal of Physics: Condensed Matter **32**, 143002 (2020).
- [11] L. Wang, M. He, F. Hardy, D. Aoki, K. Willa, F. J., and C. Meingast, *Electronic nematicity in URu₂Si₂ revisited*, (2020).
- [12] F. Bourdarot, S. Raymond, and L.-P. Regnault, *Neutron scattering studies on URu₂Si₂*, .
- [13] C. Broholm, J. K. Kjems, W. J. L. Buyers, P. Matthews, T. T. M. Palstra, A. A. Menovsky, and J. A. Mydosh, *Magnetic excitations and ordering in the heavy-electron superconductor URu₂Si₂*, Phys. Rev. Lett. **58**, 1467 (1987).
- [14] C. Broholm, H. Lin, P. T. Matthews, T. E. Mason, W. J. L. Buyers, M. F. Collins, A. A. Menovsky, J. A. Mydosh, and J. K. Kjems, *Magnetic excitations in the heavy-fermion superconductor URu₂Si₂*, Phys. Rev. B **43**, 12809 (1991).
- [15] A. Villaume, F. Bourdarot, E. Hassinger, S. Raymond, V. Taufour, D. Aoki, and J. Flouquet, *Signature of hidden order in heavy fermion superconductor URu₂Si₂: Resonance at the wave vector $q_0 = (1, 0, 0)$* , Phys. Rev. B **78**, 012504 (2008).
- [16] C. R. Wiebe, J. A. Janik, G. J. MacDougall, G. M. Luke, J. D. Garrett, H. D. Zhou, Y.-J. Jo, L. Balicas, Y. Qiu, J. R. D. Copley, Z. Yamani, and W. J. L. Buyers, *Gapped itinerant spin excitations account for missing entropy in the hidden-order state of URu₂Si₂*, Nat Phys **3**, 96 (2007).
- [17] W. Knafo, F. Duc, F. Bourdarot, K. Kuwahara, H. Nojiri, D. Aoki, J. Billette, P. Frings,

- X. Tonon, E. Lelivre-Berna, J. Flouquet, and L.-P. Regnault, *Field-induced spin-density wave beyond hidden order in URu₂Si₂*, Nature Communications **7**, 13075 (2016).
- [18] A. Pourret, A. Palacio-Morales, S. Krmer, L. Malone, M. Nardone, D. Aoki, G. Knebel, and J. Flouquet, *Fermi surface reconstruction inside the hidden order phase of URu₂Si₂ probed by thermoelectric measurements*, Journal of the Physical Society of Japan **82**, 034706 (2013).
- [19] S. Elgazzar, J. Rusz, M. Amft, P. M. Oppeneer, and J. A. Mydosh, *Hidden order in URu₂Si₂ originates from fermi surface gapping induced by dynamic symmetry breaking*, Nat Mater **8**, 337 (2009).
- [20] D. K. Morr, *Theory of scanning tunneling spectroscopy: from kondo impurities to heavy fermion materials*, Reports on Progress in Physics **80**, 014502 (2016).
- [21] P. Aynajian, E. H. da Silva Neto, C. V. Parker, Y. Huang, A. Pasupathy, J. Mydosh, and A. Yazdani, *Visualizing the formation of the Kondo lattice and the hidden order in URu₂Si₂*, Proceedings of the National Academy of Sciences **107**, 10383 (2010).
- [22] A. R. Schmidt, M. H. Hamidian, P. Wahl, F. Meier, A. V. Balatsky, J. D. Garrett, T. J. Williams, G. M. Luke, and J. C. Davis, *Imaging the fano lattice to hidden order transition in URu₂Si₂*, Nature **465**, 570 (2010).
- [23] W. Zhang, H. Y. Lu, D. H. Xie, W. Feng, S. Y. Tan, Y. Liu, X. G. Zhu, Y. Zhang, Q. Q. Hao, Y. B. Huang, X. C. Lai, and Q. Y. Chen, *ARPES/STM study of the surface terminations and 5f-electron character in URu₂Si₂*, Phys. Rev. B **98**, 115121 (2018).
- [24] F. Bourdarot, E. Hassinger, S. Raymond, D. Aoki, V. Taufour, L.-P. Regnault, and J. Flouquet, *Precise study of the resonance at $q_0=(1,0,0)$ in URu₂Si₂*, Journal of the Physical Society of Japan **79**, 064719 (2010).
- [25] S. Zhou, Y. Fu, X. Tang, S. Hu, W. Chen, and Y. Yang, *Fourier-based analysis of moiré fringe patterns of superposed gratings in alignment of nanolithography*, Opt. Express **16**, 7869 (2008).
- [26] G. Oster and Y. Nishijima, *Moiré patterns*, Scientific American **208**, 54 (1963).
- [27] J. Tersoff and D. R. Hamann, *Theory and application for the scanning tunneling microscope*, Phys. Rev. Lett. **50**, 1998 (1983).
- [28] J. Tersoff and D. R. Hamann, *Theory of the scanning tunneling microscope*, Phys. Rev. B **31**, 805 (1985).
- [29] R. D. Deegan, S. Chheda, L. Patel, M. Marder, H. L. Swinney, J. Kim, and A. de Lozanne,

- Wavy and rough cracks in silicon*, Phys. Rev. E **67**, 066209 (2003).
- [30] D. Sherman and I. Be'ery, *From crack deflection to lattice vibrations macro to atomistic examination of dynamic cleavage fracture*, Journal of the Mechanics and Physics of Solids **52**, 1743 (2004).
- [31] J. R. Kermode, L. Ben-Bashat, F. Atrash, J. J. Cilliers, D. Sherman, and A. De Vita, *Macroscopic scattering of cracks initiated at single impurity atoms*, Nature Communications **4**, 2441 (2013).
- [32] L. Zhao, D. Bardel, A. Maynadier, and D. Nelias, *Velocity correlated crack front and surface marks in single crystalline silicon*, Nature Communications **9**, 1298 (2018).
- [33] I. El Baggari, B. H. Savitzky, A. S. Admasu, J. Kim, S.-W. Cheong, R. Hovden, and L. F. Kourkoutis, *Nature and evolution of incommensurate charge order in manganites visualized with cryogenic scanning transmission electron microscopy*, Proceedings of the National Academy of Sciences **115**, 1445 (2018), <https://www.pnas.org/content/115/7/1445.full.pdf>.
- [34] J. Buhot, M. A. Méasson, Y. Gallais, M. Cazayous, A. Sacuto, F. Bourdarot, S. Raymond, G. Lapertot, D. Aoki, L. P. Regnault, A. Ivanov, P. Piekarz, K. Parlinski, D. Legut, C. C. Homes, P. Lejay, and R. P. S. M. Lobo, *Lattice dynamics of the heavy-fermion compound URu_2Si_2* , Phys. Rev. B **91**, 035129 (2015).
- [35] N. P. Butch, M. E. Manley, J. R. Jeffries, M. Janoschek, K. Huang, M. B. Maple, A. H. Said, B. M. Leu, and J. W. Lynn, *Symmetry and correlations underlying hidden order in URu_2Si_2* , Phys. Rev. B **91**, 035128 (2015).
- [36] D. R. Gardner, C. J. Bonnoit, R. Chisnell, A. H. Said, B. M. Leu, T. J. Williams, G. M. Luke, and Y. S. Lee, *Inelastic x-ray scattering measurements of phonon dynamics in URu_2Si_2* , Phys. Rev. B **93**, 075123 (2016).
- [37] S. Kambe, Y. Tokunaga, H. Sakai, T. Hattori, N. Higa, T. D. Matsuda, Y. Haga, R. E. Walstedt, and H. Harima, *Odd-parity electronic multipolar ordering in URu_2Si_2 : Conclusions from Si and Ru nmr measurements*, Phys. Rev. B **97**, 235142 (2018).
- [38] H. Suderow, I. Guillamon, and S. Vieira, *Compact very low temperature scanning tunneling microscope with mechanically driven horizontal linear positioning stage*, Review of Scientific Instruments **82** (2011), 10.1063/1.3567008.
- [39] J. A. Galvis, E. Herrera, I. Guillamón, J. Azpeitia, R. F. Luccas, C. Munuera, M. Cuenca, J. A. Higuera, N. Díaz, M. Pazos, M. Garcá-Hernandez, A. Buendá, S. Vieira, and H. Suderow,

- Three axis vector magnet set-up for cryogenic scanning probe microscopy*, Review of Scientific Instruments **86**, 013706 (2015).
- [40] D. Aoki, F. Bourdarot, E. Hassinger, G. Knebel, A. Miyake, S. Raymond, V. Taufour, and J. Flouquet, *Field re-entrant hidden-order phase under pressure in URu₂Si₂*, Journal of Physics: Condensed Matter **22**, 164205 (2010).
- [41] J. G. Rodrigo, H. Suderow, S. Vieira, E. Bascones, and F. Guinea, *Superconducting nanostructures fabricated with the scanning tunnelling microscope*, Journal of Physics: Condensed Matter **16**, R1151 (2004).
- [42] I. Horcas, R. Fernndez, J. M. Gmez-Rodrguez, J. Colchero, J. Gmez-Herrero, and A. M. Baro, *Wsxm: A software for scanning probe microscopy and a tool for nanotechnology*, Review of Scientific Instruments **78**, 013705 (2007), <https://doi.org/10.1063/1.2432410>.
- [43] <https://github.com/LowTemperaturesUAM/>.
- [44] D. Sherman, *Hackle or textured mirror?: Analysis of surface perturbation in single crystal silicon*, Journal of Materials Science **38**, 783 (2003).
- [45] G. Quinn, *Fractography of ceramics and glasses*, 10.6028/NIST.SP.960-16e2.